2009 IEEE International Conference on Robotics and Automation
Kobe International Conference Center
Kobe, Japan, May 12-17, 2009

Vision-Based Guidance and Control of a Hovering Vehicle in Unknown, GPS-denied Environments

Spencer Ahrens, Daniel Levine, Gregory Andrews, and Jonathan P. How

Abstract— **This paper describes the system architecture and core algorithms for a quadrotor helicopter that uses vision data to navigate an unknown, indoor, GPS-denied environment. Without external sensing, an estimation system that relies only on integrating inertial data will have rapidly drifting position estimates. Micro aerial vehicles (MAVs) are stringently weight-constrained, leaving little margin for additional sensors beyond the mission payload. The approach taken in this paper is to introduce an architecture that exploits a common mission payload, namely a video camera, as a dual-use sensor to aid in navigation. Several core algorithms, including a fast environment mapper and a novel heuristic for obstacle avoidance, are also presented. Finally, drift-free hover and obstacle avoidance flight tests in a controlled environment are presented and analyzed.**

I. Introduction

Recent warfighting efforts have focused increasingly on operations in dense, urban environments where GPS interference, whether unintentional or malicious, is to be expected. Simultaneously, unmanned aerial systems (UASs) have seen increasing use in military conflicts as a means to both reducing casualties and providing critical data to the warfighter. However, operations in indoor environments require the vehicle to autonomously maneuver through openings, down hallways, and around obstacles, all necessitating highly accurate position estimation and environment mapping.

While many ground vehicle solutions exist that perform autonomous indoor operations, these vehicles typically utilize multiple localization sensors at the expense of weight. UASs and especially micro aerial vehicles (MAVs) are stringently weight-constrained, with mass adversely affecting agility, endurance, and range. Yet by exploiting for the purpose of navigating through a GPS-denied environment the video feed already onboard a UAS, the camera becomes a *dual-use* sensor.

There are MAV and hover-capable MAV (HMAV) systems currently under development that address the autonomous flight problem for indoor, GPS-denied, or unknown environments. Forward flight MAVs that use optical flow for obstacle avoidance have demonstrated robust flight stability and collision avoidance in small flight spaces, however, they neither map the 3D environment nor accurately estimate position [1], [2], [3].

Refs. [4] and [5] present quadrotor MAV solutions that utilize downward-looking cameras to enable drift-free autonomous hover. Although very capable in the hands of a human pilot, these solutions: are incapable of estimating absolute position while traversing unknown environments; cannot map obstacles; and, thus, cannot navigate unknown environments autonomously.

Ref. [6] demonstrates the utility of LIDAR onboard HMAVs for position estimation in indoor environments. These systems show promise for HMAV development with the continuing miniaturization of LIDAR modules, yet they currently require prior maps of the environment to enable registration of measurements, and position estimates are too noisy to accurately estimate velocity for effective control feedback. Ref. [7] demonstrates accurate simultaneous localization and mapping of corner features, although the methods used are specific to unobstructed hallways and are not formulated for absolute position estimation. Given this prior work, the primary contributions of this paper are the system architecture and key supporting algorithms for vision-based guidance and control of an HMAV in unknown, indoor environments [8].

II. Hardware Architecture

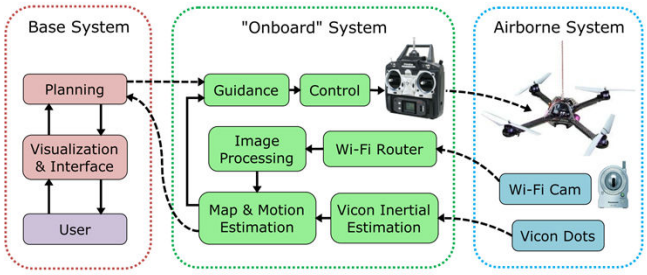

Fig. 1. Diagram of the hardware architecture.

The basic hardware structure is outlined in Fig. 1. The airborne system consists of the vehicle, the wireless camera, and reflective infrared markers (dots). The conceptually "onboard" system is composed of a regular desktop computer, a Wi-Fi router for communication with the onboard camera, and a Vicon motion capture system for emulating inertial data. The base station is composed simply of a separate desktop computer workstation. For ease of prototyping, and in an effort to eschew the development of custom vehicles and electronics, as much computation is done offboard as possible. At the same time, extensive process timing analysis is done in order to analyze the feasibility of the core algorithms to ultimately run in real-time on an embedded system. The airborne system and the emulated onboard system are described in detail in the following sections.

The first, second, and fourth authors are members of the Aerospace Controls Laboratory, Massachusetts Institute of Technology, 77 Massachusetts Ave., Cambridge, MA 02139. jhow@mit.edu

The third author is an engineer at the Charles Stark Draper Laboratory, Inc., 555 Technology Square, Cambridge, MA 02319.

A. Vehicle

The HMAV chosen for this research is the Hummingbird quadrotor, which is outfitted with an embedded electronics suite, from Ascending Technologies [9], [10]. An onboard 8-bit microcontroller samples and fuses the data of a 6-axis IMU at 1 kHz to generate a tilt estimate used for onboard tilt stabilization. The digital communication channel (when connected, for example, with an xBee-Pro digital radio) allows external access to the IMU readings and tilt estimates. Any external controller need only specify the desired tilt angle; the vehicle, which receives control signals via a standard 72 MHz R/C receiver, will track this reference with high performance.

B. Imaging Sensor

The imaging sensor selected is a Wi-Fi enabled Panasonic BL-C131A network camera, which hosts 320x240 pixel images that are retrieved at 15–20 Hz through the network as JPEG files and loaded into the image processing system. The 1mm diameter lens has a 41° vertical and 53° horizontal FOV.

Experience has shown that digital wireless cameras are better suited for machine vision applications than their analog counterparts, which suffer indoors from multi-path interference and thereby produce images with distortions and lines of static [11]. The sensor used in this experiment produces images with JPEG compression artifacts that degrade image quality yet are consistent enough to not disturb frame-to-frame processing routines.

C. RAVEN and Emulated Inertial Data

The MIT Real-time indoor Autonomous Vehicle test ENvironment (RAVEN) [12], [13] provides the hardware foundation for the developments presented. RAVEN combines the tracking capabilities of a Vicon-MX camera system [14] with R/C hardware and an array of networked servers, comprising an ideal rapid-development environment.

The estimation filter of the conceptually onboard system takes IMU data and camera images as inputs. Although the vehicle is equipped with a digital radio to access IMU data, communication dropouts and transmission corruption severely impair the ability of the estimation filter to accurately estimate vehicle ego-motion. Therefore RAVEN is used to emulate inertial data in all flight tests presented. The outputs of RAVEN's Vicon system are the vehicle position and an attitude quaternion, each of which is passed through an Extended Kalman Filter (EKF) to emulate accelerometer and gyroscope data, respectively.

Figs. 2 and 3 compare the hardware IMU data to filtered Vicon data and indicate the former to be less reliable than the latter, due to the existence of a wireless data link and as typified by the spikes and dropouts in Fig. 2. Despite this, both the hardware and filtered Vicon data have similar nominal behavior. The root mean square (RMS) noise levels of the hardware IMU data are 0.028 m/s^2 and 0.89 deg/s; the Vicon RMS are slightly higher, at 0.037 m/s^2 and 0.96 deg/s.

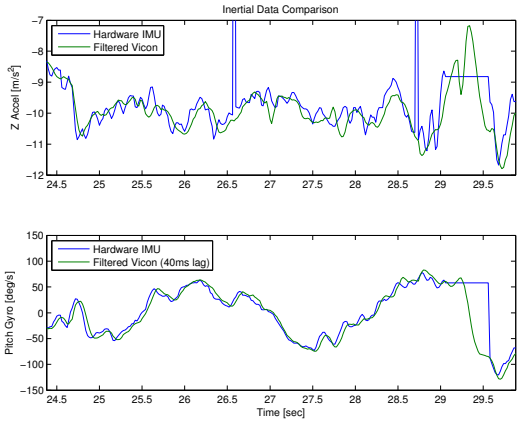

Fig. 2. Comparison between inertial data measurement systems. Note dropout between 29 and 29.5 seconds.

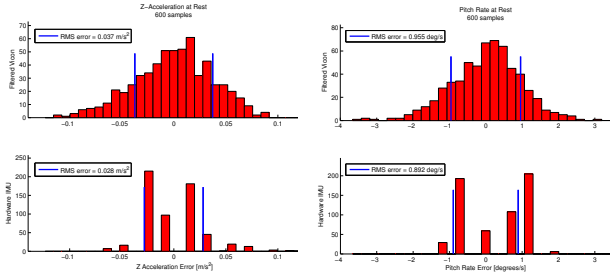

(a) Z-axis acceleration. (b) Pitch-axis rotation rate.

Fig. 3. At-rest inertial data comparison.

Filtering also incurs an additional lag over hardware data, e.g., 40 ms for gyroscope data.

Discretization of the IMU data, clearly shown by the wide gaps between bars in Fig. 3, is due to the fixed precision of the embedded electronics, which evaluates to 0.020 m/s^2 and 0.61 deg/s in physical terms. However, because the magnitudes of the RMS noise levels and the operational values are larger than the respective fixed precisions, the discretization should not significantly affect the performance of the filter.

Because of the close match of noise characteristics and knowledged of the penalties incurred by using filtered Vicon data, it is expected that the existing ego-motion estimation system likely would operate with similar, if not higher, performance when implemented on an embedded system. Finally, because Vicon has sub-millimeter position accuracy, its unfiltered data can be used off-line as truth for the purposes of measuring estimation errors.

III. Imaging, Estimation, & Mapping

A. Image Processing

Visual perception is essential to system performance, as it remains the vehicle's exclusive capability in sensing the environment and is a direct function of the absolute position and orientation. Conversely, inertial data only provide an indication of rates and tilt.

The primary tasks of image processing are the detection and maintenance of features of interest, or points in space that correspond to locations in the images. To this end, low-level image processing technologies of the Open Computer

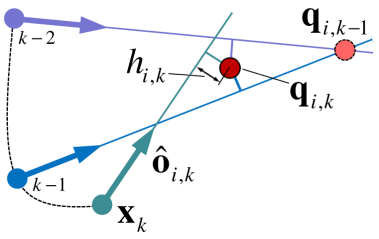

Fig. 4. Vision bearings as the vehicle traverses dashed path.

Vision Library (OpenCV) [15] are utilized. The Shi-Tomasi "good features to track" detector [18] finds points with large eigenvalues of the image gradient in multiple directions. In order to achieve feature spread across the image, which is advantageous for the purposes of navigation (i.e., yield a low position dilution of precision [20]), a mask is erected in the vicinity of existing features, within which new features are not detected. The pyramidal Lucas-Kanade optical flow calculator [16], [17] compares pixel patches in successive images in an attempt to accurately maintain the locations of features detected in previous images.

Once tracking is performed, the remaining features are scanned; those that are clumped together, have jumped, or have poorly converging 3D position estimates are discarded and replaced in subsequent calls to the detector. The ultimate result of feature tracking is the delivery of feature locations to the estimation filter and the fast environment mapper, which are discussed next.

B. Ego-Motion Estimation

The process for ego-motion estimation was developed in collaboration with Draper Laboratory [19] building in part on [21], [22]. The EKF used in this implementation accounts for: the position, velocity, and attitude of the vehicle; biases in all axes of the accelerometer and gyroscope; and position of initial sighting, horizontal bearing, vertical bearing, and range of all features.

C. Fast Environment Mapping

While the ego-motion estimation filter explicitly estimates feature locations, it is computationally expensive; thus, only a small number of features can be tracked at once. An alternative method employs a simple least-squares pseudo-intersection algorithm, is well suited for mapping many features, and gives a more complete view of the world than that given by the features in the estimation filter.

Fig. 4 shows the formulation for optimally estimating the pseudo-intersection point $\mathbf{q}_{i,k}$ of obstacle i at time k. In the figure, $\mathbf{x}_k$ is the estimated vehicle position, $\hat{\mathbf{o}}_{i,k}$ is the corresponding unit vector bearing estimate from the vehicle to feature i, and $h_{i,k}$ is the minimum distance from $\mathbf{q}_{i,k}$ to the estimated vision ray. The two previous bearing estimates at times $k-1$ and $k-2$ show the approximate nature of the intersection.

A simple least-squares algorithm efficiently computes the best-fit intersection point $\mathbf{q}_{i,k}$ by minimizing Σh^2. Originally formulated by Bethke in [23] for simultaneous measurements from multiple vehicles tracking the same target, the algorithm is adapted here to the single vehicle case, where each measurement i is taken at a different point in time. Because the vehicle position estimate tends to drift, an exponential decay of parameter α that slowly attenuates the contributions of older measurements can be incorporated into the transition. The recursive update equations for obstacle i at the current timestep k, with $\mathcal{A}_{i,0}$ and $\mathbf{b}_{i,0}$ initialized to zero, are

$$\mathcal{A}_{i,k} = \alpha\mathcal{A}_{i,k-1} + (I - \hat{\mathbf{o}}_i\hat{\mathbf{o}}_i^T) \quad (1)$$

$$\mathbf{b}_{i,k} = \alpha\mathbf{b}_{i,k-1} + (\mathbf{x}_k - (\mathbf{x}_k \cdot \hat{\mathbf{o}}_i)\cdot\hat{\mathbf{o}}_i) \quad (2)$$

$$\mathbf{q}_{i,k} = \mathcal{A}_{i,k}^{-1}\mathbf{b}_{i,k}. \quad (3)$$

For each feature, we need only store the 3x3 $\mathcal{A}$ matrix and 3-element $\mathbf{b}$ vector and update them with a constant time expression, independent of the number of measurements we have accumulated over time. We can also express each feature's confidence as $c = \sum_{j=1}^{k}\|\Delta\mathbf{x}_j\|/\|\Delta\mathbf{q}\|$ where the estimate jitter $\|\Delta\mathbf{q}\|$ is simply the magnitude of the difference between the current and previous estimates $\mathbf{q}$. Taking the distance moved since the last update $\|\Delta\mathbf{x}_i\|$ as approximately $\|\mathbf{v}\Delta t\|$, the confidence can be recursively updated as

$$\tilde{c}_{i,k} = \tilde{c}_{i,k-1} + \|\mathbf{v}\Delta t\| \quad \Rightarrow \quad c_{i,k} = \frac{\tilde{c}_{i,k}}{\|\mathbf{q}_{i,k} - \mathbf{q}_{i,k-1}\|}. \quad (4)$$

Once computed, these confidences determine both whether a feature is used for obstacle avoidance and (in the case of sufficiently low confidence) whether that feature is due to be culled from the map should its confidence not improve during a predefined grace period.

D. Flight Control Issues

The primary difficulty with vision-in-the-loop estimation is that estimate errors decrease control performance, generally via oscillations. These oscillations cause the camera view to change constantly, which forces features to go out of view more often, reducing their persistence. With low-light indoor conditions and low camera quality, the high rate of movement also causes the images to blur. Decreased vision fidelity begets further estimate degradation, and a positive feedback loop is formed as the control performance and estimation subsequently decline.

IV. Obstacle Avoidance

A lightweight reactive obstacle avoidance heuristic for the purpose of indoor navigation in complex, unknown environments is now presented. Fast, effective, and natively three-dimensional, the heuristic is easily tractable onboard existing micro flight controllers. As the formulas are of closed form, sampling, which typically requires compromise between completeness and speed (especially when working in three dimensions [24]), is not necessary.

The algorithm takes as inputs the environment map generated using the extended fast-mapping technique (Section III-C), the goal position, and the vehicle's *reference* state; it generates as an output a reactive acceleration component $\mathbf{a}_r$. By utilizing the vehicle's reference state rather than its

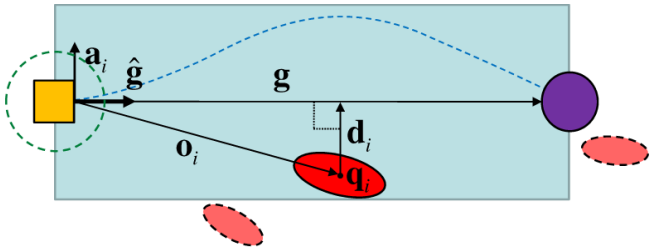

Fig. 5. Collision corridor with two obstacles outside the corridor (dashed ellipses) ignored. The corridor is a three-dimensional cylinder, flattened in this diagram to facilitate discussion.

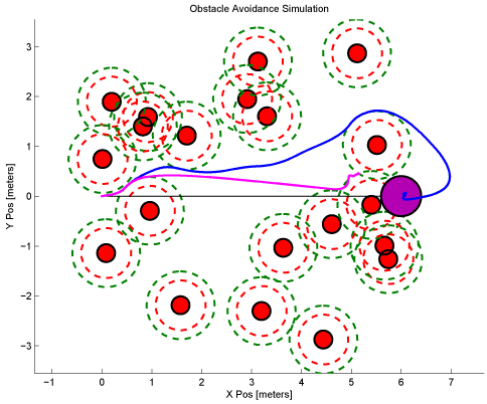

Fig. 6. Comparison of a "repulsion only" (no anticipation) trajectory in magenta versus the corridor-augmented method trajectory in blue, with 20 obstacles in the plane $z = 0$.

estimated state, the algorithm becomes deterministic given a goal and a set of obstacle locations. Thus, trajectory generation is decoupled from control and estimation performance; such coupling would otherwise cause undesirable feedback. The same methodology was successfully employed by MIT in the DARPA Urban Challenge [25].

Fig. 5 shows a 2D cutaway diagram of a typical obstacle-avoiding trajectory. The vector from the vehicle at $\mathbf{x}$ to the goal is $\mathbf{g}$ (normalized to $\hat{\mathbf{g}}$), and the vector from the vehicle to the obstacle i with position estimate $\mathbf{q}_i$ is $\mathbf{o}_i$. The ith cross-goal vector $\mathbf{d}_i$ is the shortest segment from obstacle i to $\mathbf{g}$, such that

$$\mathbf{d}_i = (\hat{\mathbf{g}} \cdot \mathbf{o}_i) \cdot \hat{\mathbf{g}} - \mathbf{o}_i \quad \text{with} \quad \mathbf{o}_i = \mathbf{q}_i - \mathbf{x}. \tag{5}$$

The avoidance buffer of an obstacle r_{buf}, within which the vehicle will try to reverse itself, subsumes the vehicles radius r_{veh}. If $\exists i$ such that $r_{veh} < \|\mathbf{q}_i - \mathbf{x}\| < r_{buf}$, the vehicle has not crashed but is in the avoidance buffer of a feature, the reactive acceleration can be immediately set to $\mathbf{a}_r = -a_{\max}\hat{\mathbf{o}}_i$, where $a_{\max}$ is a maximum reactive acceleration magnitude.

The distance x_{stop} that vehicle will travel towards an object given the current velocity $\mathbf{v}$ is calculated from simple kinematics as $x_{stop} = (\mathbf{v} \cdot \hat{\mathbf{o}}_i)^2/(2a_{\max})$. At time k, for the purposes of navigating between $\mathbf{x}_k$ and $\mathbf{x}_k + \mathbf{g}$, we consider only those obstacles that: have a confidence c_i above a set threshold; are within a cylindrical "corridor" of $\mathbf{g}$; are in front of the vehicle; and are closer than the goal to the vehicle. Formally, we express the "avoidance criteria," respectively, for obstacle i as

$$\left.\begin{array}{rcl} c_i & > & c_{\min} \\ \|\mathbf{d}_i\| & < & 2(r_{buf} + x_{stop}) \\ \|\mathbf{o}_i\| & < & \|\mathbf{g}\| \\ \mathbf{o}_i \cdot \mathbf{g} & > & 0 \end{array}\right\} \tag{6}$$

For an obstacle that meets the avoidance criteria, its contribution to the reactive acceleration direction vector $\mathbf{a}_a$ is composed of its cross-goal vector $\mathbf{d}_i$, which by construction is orthogonal to $\mathbf{g}$, and is inversely weighted by the time-to-impact t_i. If there are n obstacles that meet the avoidance criteria, the final reactive acceleration $\mathbf{a}_r$ is aligned with $\mathbf{a}_a$ and has a magnitude proportional to the velocity to the nearest obstacle and inversely proportional to an acceleration time constant τ_r. More compactly,

$$t_i = \frac{\|\mathbf{o}_i\|}{\hat{\mathbf{o}}_i \cdot v} \tag{7}$$

$$\mathbf{a}_a = \left[\sum_{i=1}^{n} \frac{\|\mathbf{d}_i\|\hat{\mathbf{d}}_i}{t_i}\right] = \left[\sum_{i=1}^{n} \frac{\mathbf{d}_i}{t_i}\right] \tag{8}$$

$$\mathbf{a}_r = 1.5\frac{\|\mathbf{o}_j\|}{t_j \tau_r}\hat{\mathbf{a}}_a, \quad \text{with } j = \text{argmin}_i\, t_i. \tag{9}$$

This heuristic generates a reference reactive acceleration $\mathbf{a}_r$ that can be combined with a goal-seeking acceleration $\mathbf{a}_g$ and an orbital cancelation acceleration $\mathbf{a}_c \perp \mathbf{a}_g$ such that $\mathbf{a} = \mathbf{a}_g + \mathbf{a}_c + \mathbf{a}_r$. The orbital cancelation term can very simply be found to be

$$\mathbf{a}_c = \frac{\hat{\mathbf{g}} \cdot (\mathbf{v} \cdot \hat{\mathbf{g}}) - \mathbf{v}}{\tau_c} \tag{10}$$

for some acceleration time constant τ_c. While $\mathbf{a}_g$ is always along $\hat{\mathbf{g}}$, the scheduling of its magnitude is less trivial and is left to the implementer. Note that in the case of an emergency reverse, the vehicle can use just reactive acceleration references and impose $\mathbf{a}_c = \mathbf{a}_g = \underline{0}$. A simulation of randomly generated obstacles (merely for ease of presentation, in the plane $z = 0$) is shown in Fig. 6.

V. Flight Test Results

A. Drift-Free Hover

When hovering, the vehicle maintains an almost fixed point of view, maximizing feature persistence and minimizing drift. Fig. 7 shows data from a typical hover using the vision-based state estimate for control feedback. Because the vehicle remains in the same approximate location, no features are lost, and, thus, the average drift for the 96 seconds the vehicle is commanded to hover is negligible. The RMS of the error in the inertial X axis, for example, is 7.61 centimeters.

By contrast, if vision data is not incorporated and the estimator must rely strictly on the IMU, the position estimate quickly diverges (i.e., $\|\mathbf{x}\| \to \infty$) while the vehicle is still on the ground and waiting to take off. This is result of the estimator performing a double integration on biases and noise in the accelerometer measurements.

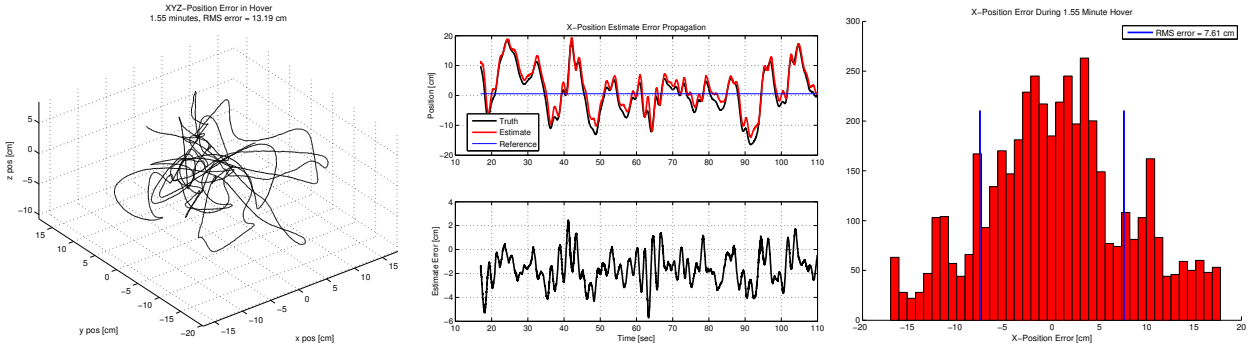

(a) 3D plot of flight.

(b) Propagation of X position error.

(c) Distribution and RMS error in X truth position deviation from the reference.

Fig. 7. Simple closed-loop hover using vision-based state estimation for state feedback.

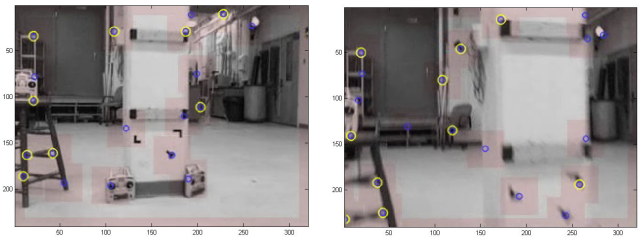

(a) The environment.

(b) Approaching the stool.

Fig. 8. Onboard camera view of the final environment setup for autonomous obstacle avoidance. The circles superimposed on the image indicate features of interest used for navigation and guidance.

B. Vision-Based Control and Obstacle Avoidance

As can be seen in Fig. 8, the environment was set up with the pole, a bar stool, and additional clutter in the center of the room, leaving enough space for the vehicle to maneuver, but with a clear and complex obstacle set blocking the direct path to the goal.

Fig. 9(a) shows two plots from the top (x,y) and side (z,y) of a successful obstacle avoidance flight. The green circle is the take-off point, the crosses are the landing points, and the purple spots represent a snapshot in time of the features used for obstacle avoidance; a cylinder and a cuboid, representing the obstacles, have been superimposed in the operator's view of Fig. 9(b) for demonstrative purpose. As the vehicle attempted to move toward the goal, the obstacle avoidance commanded to fly the vehicle up, around the pole to the left, over the stool, and down to a smooth touchdown near the goal.

It is of interest to note that the during the 5 m flight, the position estimate drifted by approximately 1 m, but the vast majority of error was accumulated just as the vehicle passed over the stool, corresponding with the discarding of all features associated with the obstacle. This would indicate that future trajectory generators should allow the camera to be pointed along a bearing other than the direction of movement, as was imposed in this experiment.

Fig. 10 shows orthographic and operator views of a test flight with the same starting conditions and goal state as with the test previously discussed. However, due to a difference in absolute position at the time the waypoint command was given, the navigation system plans a trajectory to the East, around the pole, avoiding the stool entirely. The data visible in the figure is a clear example of the complimentary offset errors that develop in both the feature estimates and the estimated vehicle position.

VI. Conclusion

This paper has focused on the higher level system architecture and key supporting algorithms for the guidance and control of an HMAV in unknown, GPS-denied environments. The concepts and methodologies for image processing are discussed, and the implementations of the environmental mapping and reactive obstacle avoidance algorithms are presented. Flight results of the autonomous system are analyzed, demonstrating the viability of this solution to achieve its objectives in real environments on physical hardware. Although developed in a testbed for ease of prototyping, many of the issues involving the transition to embedded flight systems are directly addressed, with promising conclusions for the ultimate real-world implementation of these contributions.

VII. Acknowledgments

Research supported by Draper Laboratory and by AFOSR DURIP FA9550-07-1-0321.

References

[1] T. Netter and N. Francheschini, "A robotic aircraft that follows terrain using a neuromorphic eye," *IEEE/RSJ Intl. Conf. Intelligent Robots and System*, 1:129-134, 2002.

[2] F. Ruffier and N. Franceschini, "Visually guided micro-aerial vehicle: automatic take off, terrain following, landing and wind reaction," *IEEE Intl. Conf. Robotics and Automation*, 3:2339-2346, 26 April-1 May 2004.

[3] J.-C. Zufferey and D. Floreano, "Fly-inspired visual steering of an ultralight indoor aircraft," *IEEE Trans. Robotics*, 22(1):137-146, February 2006.

[4] S.G. Fowers, D.-J. Lee, B.J. Tippetts, K.D. Lillywhite, A.W. Dennis, and J.K. Archibald, "Vision aided stabilization and the development of a quad-rotor micro UAV," *Intl. Symp. Computational Intelligence in Robotics and Automation*, pp. 143-148, 20-23 June 2007.

[5] AirRobot, Gmbh. Available at http://www.airrobot.de, 2008.

[6] R. He, S. Prentice, and N. Roy, "Planning in Information Space for a Quadrotor Helicopter in a GPS-denied Environment", *IEEE Intl. Conf. Robotics and Automation*, Pasadena, California, May 2008.

[7] K. Celik, S.J. Chung, and A.K. Somani, "MVCSLAM: Mono-Vision Corner SLAM for Autonomous Micro-Helicopters in GPS Denied Environments", *AIAA Guidance, Navigation, and Control Conf.*, Honolulu, Hawaii, August 2008.

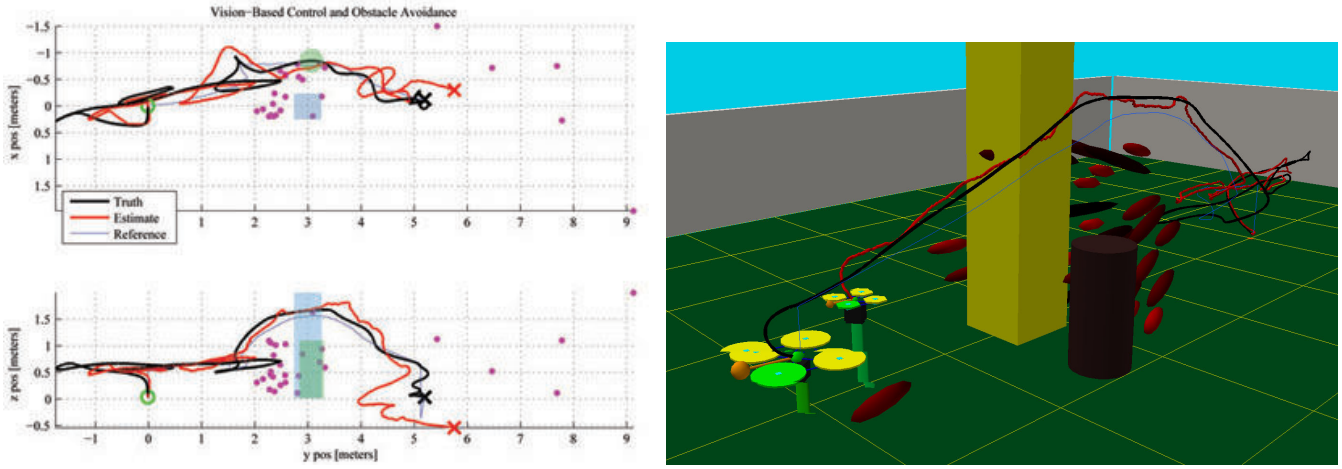

(a) Orthographic views. (b) Operator's 3D visualization.

Fig. 9. Flight over the stool from three perspectives.

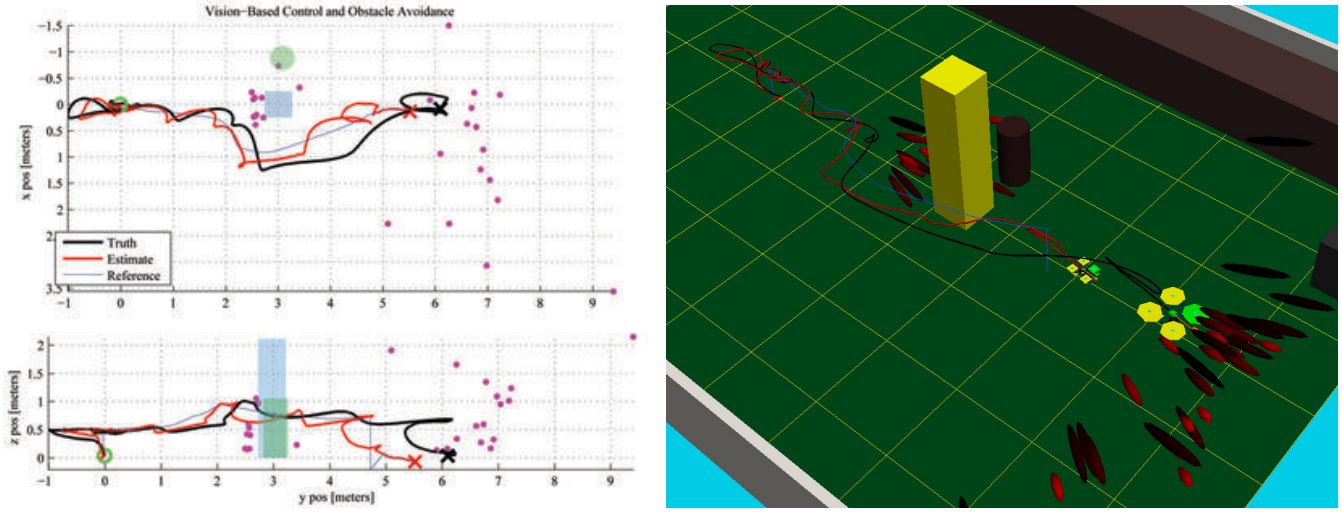

(a) Orthographic views. (b) Operator's 3D visualization.

Fig. 10. Flight around pole from three perspectives.

[8] S. Ahrens, "Vision-Based Guidance and Control of a Hovering Vehicle in Unknown Environments," Master's thesis, Massachusetts Institute of Technology, 2008.

[9] Ascending Technologies. AscTec Hummingbird Quadrocopter. Available at htpp://www.asctec.de, 2008.

[10] D. Gurdan, J. Stumpf, M. Achtelik, K.-M. Doth, G. Hirzinger, and D. Rus, "Energy efficient autonomous four-rotor flying robot controlled at 1 kHz," *IEEE Intl. Conf. Robotics and Automation*, pp. 361-366, 10-14 April 2007.

[11] B. Bethke, M. Valenti, and J.P. How, "Cooperative Vision Based Estimation and Tracking Using Multiple UAVs," *Conf. Cooperative Control and Optimization*, Gainesville, FL, January 2007.

[12] J.P. How, B. Bethke, A. Frank, D. Dale, and J. Vian, "Real-time indoor autonomous vehicle test environment," *IEEE Controls System Magazine*, pp. 51-64, April 2008.

[13] M. Valenti, B. Bethke, G. Fiore, J.P. How, and E. Feron, "Indoor multi-vehicle flight testbed for fault detection, isolation, and recovery," *AIAA Guidance, Navigation, and Control Conf.*, Keystone, CO, August 2006.

[14] Vicon Company. Vicon Motion Capture Systems. Available at http://www.vicon.com/, 2007.

[15] Intel Corporation. OpenCV Computer Vision Library. Available at http://www.intel.com/technology/computing/opencv/, 2007.

[16] J.-Y. Bouguet, "Pyramidal Implementation of the Lucas Kanade Feature Tracker," http://robots.stanford.edu/cs223b04/algo_tracking.pdf, 2000.

[17] B.D. Lucas and T. Kanade, "An iterative image registration technique with an application to stereo vision," *Proc. 7th International Joint Conference on Artificial Intelligence*, pp. 674-679, April 1981.

[18] J. Shi and C. Tomasi, "Good features to track," *IEEE Conf. Computer Vision and Pattern Recognition*, pp. 593-600, 1994.

[19] R.W. Madison, G.L. Andrews, P.A. DeBitetto, S.A. Rasmussen, and M. S. Bottkol. Vision-aided navigation for small UAVs in GPS-challenged environments. In *AIAA Infotech at Aerospace Conference and Exhibit*, May 2007.

[20] M.S. Grewal, L.R. Weill, and A.P. Andrews, *Global Positioning Systems, Inertial Navigation, and Integration*, John Wiley & Sons, Inc., New York, NY; 2001.

[21] J. Civera, A. Davison, and J. Montiel, "Inverse depth to depth conversion for monocular SLAM," *IEEE Intl. Conf. Robotics and Automation*, 10-14 April 2007.

[22] J. Montiel, J. Civera, and A. Davison, "Unified inverse depth parametrization for monocular SLAM," *Robotics: Science and Systems*, August 2006.

[23] B. Bethke, "Persistent vision-based search and track using multiple UAVs," Master's thesis, Massachusetts Institute of Technology, 2007.

[24] E. Rimon and D.E. Koditschek, "Exact robot navigation using artificial potential functions," *IEEE Trans. Robotics and Automation*, 8(5):501-518, October 1992.

[25] Y. Kuwata, J. Teo, S. Karaman, G. Fiore, E. Frazzoli, and J.P. How, "Motion planning in complex environments using closed-loop prediction", *AIAA Guidance, Navigation, and Control Conf.*, Honolulu, Hawaii, August 2008.